

Underluminous tidal disruption events

Pau Amaro Seoane¹ *

Universitat Politècnica de València, Spain

Max-Planck-Institute for Extraterrestrial Physics, Garching, Germany

Higgs Centre for Theoretical Physics, Edinburgh, UK

Kavli Institute for Astronomy and Astrophysics, Beijing 100871, China

draft 26 July 2023

ABSTRACT

We have evidence of X-ray flares in several galaxies consistent with a star being tidally disrupted by a supermassive black hole (MBH). If the star starts on a nearly parabolic orbit relative to the MBH, one can derive that the fallback rate follows a $t^{-5/3}$ decay in the bolometric luminosity. We have modified the standard version of the smoothed-particle hydrodynamics (SPH) code GADGET to include a relativistic treatment of the gravitational forces. We include non-spinning post-Newtonian corrections to incorporate the periastris shift and the spin-orbit coupling up to next-to-lowest order. We run a set of simulations for different penetration factors in both the Newtonian- and the relativistic regime. We find that tidal disruptions around MBHs in the relativistic cases are underluminous for values starting at $\beta \gtrsim 2.25$; i.e. the fallback curves produced in the relativistic cases are progressively lower compared to the Newtonian simulations as the penetration parameter increases. This is due to the fact that, contrary to the Newtonian cases, we find that all relativistic counterparts feature a survival core for penetration factors going to values as high as 12.05. We derive a relativistic calculation which shows that geodesics of the elements in the star converge as compared to the Newtonian case, allowing for a core to survive the tidal disruption. A survival core should consistently emerge from any TDE with $\beta \gtrsim 2.25$. The higher the value, the lower the colour temperatures than derived from standard accretion models.

Key words: transients: tidal disruption events – relativistic processes – quasars: supermassive black holes

1 MOTIVATION

A star passing very close to a massive black hole (MBH) may be torn apart because of the tidal effects, and the interaction of the stellar debris in the vicinity of the black hole will give rise to a burst of electromagnetic radiation. The characteristics of this tidal disruption event (TDE), such as its temperature, peak luminosity, and decay timescale, are functions of the mass and spin of the central MBH. The subsequent accretion of the debris gas by the black hole produces additional emission, and lead to phases of bright accretion that may reveal the presence of a MBH in an otherwise quiescent galaxy (see e.g. Wheeler 1971; Hills 1975; Frank & Rees 1976; Carter & Luminet 1982, 1983; Rees 1988a; Murphy et al. 1991; Magorrian & Tremaine 1999; Syer & Ulmer 1999; Freitag & Benz 2002; Gezari et al. 2003; Wang & Merritt 2004), with rates which vary depending on various factors, but of the order of $10^{-5} - 10^{-6} \text{ yr}^{-1}$ (see e.g.

Rees 1988b and Stone et al. 2020 for a recent review on the rates and characteristics). These phenomena can be used as a probe of accretion physics close to the event horizon (Brennan 2013; Reynolds 2014).

Many disruption candidates have already been detected with ROSAT, Chandra, Swift (see e.g. <https://tde.space>), and the ZTF (van Velzen et al. 2020) and the number will surge with upcoming transient surveys like the Large Synoptic Survey Telescope (LSST), SRG/eROSITA (Khabibullin et al. 2014), as well as the ESA L2 mission Athena (Nandra et al. 2013).

A conundrum related to optically-discovered TDEs is that their color temperatures are significantly below the values predicted by theoretical models (Gezari et al. 2012; Chornock et al. 2014; Holoien et al. 2014; van Velzen & Farrar 2014; Arcavi et al. 2014). Observations depict a temperature and bolometric luminosity well below theoretical predictions based on accretion, and based on the same model, the derived black-body emission radius implies an orbital motion below the expected theoretical values. In general,

* E-mail: amaro@riseup.net (PAS)

the fallback model requires masses much less than a solar mass in order to explain the difference in luminosity of the observed flares and the theoretical expectations.

Different theoretical models have been put forward to explain this fact. The work of Li et al. (2002) suggested that the low luminosity may indicate that the disrupted star is a brown dwarf or a planet. An alternative explanation is that the assumption that the gas immediately circularizes when it comes back close the MBH is not accurate, and could trigger internal shocks that would result into a reduced luminosity. In particular, Piran et al. (2015) suggested that the released energy during the process of circularisation, and not that accreted on to the MBH, is responsible for the observed optical TDE candidates. More recently, Zhou et al. (2020) argued that the disk does not circularize and remains eccentric, which as a consequence leads the orbital energy of the stellar debris to be advected on to the MBH without being radiated away.

In this work we show with a set of smoothed-particle hydrodynamics (SPH) simulations with relativistic corrections that unbound stars lead to partial disruptions, which naturally explain the difference in the observed luminosity, for penetration values as deep as $\beta = 12.05$.

2 RELATIVISTIC IMPLEMENTATION

Relativistic effects have been considered in the related literature by e.g. Tejeda et al. (2017), which implemented a relativistic description of the evolution of the hydrodynamical elements with a quasi-Newtonian treatment of the fluid's self-gravity.

Earlier this year, Ryu and collaborators presented a series of works which also address TDEs in a relativistically fashion. For this approach they depart from the intrinsically-conservative GR hydrodynamical numerical code of Noble et al. (2009) designed to study magnetohydrodynamic (MHD) turbulence in accretion disks around MBHs. To study TDEs, they assume that spacetime is Schwarzschild plus contributions from the star self-gravity, and the dynamics of the star is described by hydrodynamics, solving the general-relativistic energy-momentum equations in the Schwarzschild background. This hence implies that in the absence of material forces the fluid elements strictly follow geodesics. The self-gravity of the star is described in the weak field, taking into account only the Newtonian gravitational potential. They then evolve the hydrodynamical equations in a frame where the metric is nearly flat and move the whole system in a rigid way along the orbit using parallel transport of the local frame. Hence, it is the trajectory of the system what “sees” the Schwarzschild metric but the fluid elements almost live in a flat spacetime.

More precisely, they consider a modified metric, $\tilde{g}_{\mu\nu} = g_{\mu\nu} + h_{\mu\nu}$, with $g_{\mu\nu}$ the Schwarzschild metric and $h_{\mu\nu}$ accounts for the self-gravity of the star. They assume the self-gravity is weak, so that the only non-zero component of the self-gravity perturbations is the time-time one: $h_{tt} = -2\Phi_{sg}/c^2$, where Φ_{sg} is the Newtonian potential of the star, in the sense that it satisfies a Poisson equation where the mass density is replaced by the star proper rest-mass density. The procedure to incorporate this self-gravity is a bit more intricate than adding it to the Schwarzschild metric. The

assumptions made to compute the self-gravity contribution include that the metric of Schwarzschild should not deviate from the Minkowski metric. Here is where the intricacy mentioned comes, since they need a parallel-transported tetrad adapted to the star as mentioned before, so that in that frame the assumptions made are valid. It is important to note that they separate the problem of solving the hydrodynamical equations from the motion of the star around the MBH. This can be envisaged as having a frame center at the (center of mass) star where the metric, in an orthonormal basis, is exactly Minkowski (deviating as we move from the center of mass). Then they solve the hydrodynamical equations in this frame and the motion of the star is “rigid” (only the center of mass moves) according to the parallel-transport equations for the orthonormal basis (see Ryu et al. 2020b). In their calculations all stars have net bound orbits by an amount of the order $\sim 10^{-10}c^2 \sim 10^{-3}(\sigma^2/2)$, where σ is the bulge dispersion and c the speed of light.

With this scheme they investigate TDEs in four additional works. In Ryu et al. (2020a) they find that the critical pericenter distance for full disruptions is enhanced by up to a factor of ~ 3 as compared to the Newtonian case, and that it depends on the mass of the star in a non-trivial way (see Guillochon & Ramirez-Ruiz 2013, for previous work). The results of Ryu et al. (2020c) regarding partial disruptions show that due to the little mass distributed at low energies, late-time fallback is suppressed. The mass return rate should then be $\propto t^{-p}$ with $p \in [2, 5]$ in partial disruptions. In Ryu et al. (2020d) they show that relativistic effects induce width delays in the debris energy so that the magnitude of the peak return rate decreases. These results had already been pointed out by the previous work of Ivanov & Chernyakova (2006); Kesden (2012); Servin & Kesden (2017), although Ryu and collaborators provided quantitative corrections to these previous treatments. In Krolik et al. (2020) they discuss the event rates and the fate of the rest of the star which is not disrupted (i.e. the amount of mass still inside the computational box when they stopped the simulation), which might interact with the MBH on a second periaapsis passage or rejoin the stellar cluster.

In this work we modify the acceleration computation of GADGET (Springel 2005) to include relativistic corrections, which are based on the post-Newtonian (PN) formalism for the interaction between two bodies (in our case each of the hydrodynamical particles and the MBH). This means that we simply add relativistic correcting terms to the Newtonian gravitational forces calculated between the MBH and the hydrodynamical particles that form the star during the whole simulation, which initially is set on a completely unbound orbit. This approximation allows us to capture the relativistic effects while allowing us to study the evolution of the star to larger radii without any other approximation than those inherent to SPH methods and the post-Newtonian expansion, valid in this regime of low (but yet relativistic) velocities. In this regard, our scheme is self-consistent and all phenomena related to relativistic effects and hydrodynamics emerge naturally by integrating the system.

The relative acceleration, in the center-of-mass form, including all PN corrections can be written in the following way:

$$\frac{d\vec{v}}{dt} = -\frac{Gm}{r^2}[(1+A)\vec{n} + B\vec{v}] + \vec{C}_{1.5,SO} \quad (1)$$

In this equation $\vec{v} = \vec{v}_1 - \vec{v}_2$ is the relative velocity vector, $m = M_\bullet + m_{\text{gas}}$ the total mass, with M_\bullet the mass of the MBH and m_{gas} the mass of a gas particle, r the separation and $\vec{n} = \vec{r}/r$. A and B are coefficients that can be found in Blanchet & Iyer (2003). Since we are modelling extremely light gas particles around a MBH, we adopt the terms in the limit $m_{\text{gas}} = 0$. We consider the leading order spin-orbit interaction, with the term $\vec{C}_{1.5,SO}$ in which the subscript SO stands for spin-orbit coupling, which can be found in (Tagoshi et al. 2001; Faye et al. 2006), and the first post-Newtonian correction to periaapsis shift. We do not include dissipative terms because, contrary to an extreme-mass ratio inspiral (Amaro-Seoane 2018), the star only has one periaapsis passage, and the gravitational radiation can be neglected. All the PN interactions are only considered between a gas particle and the MBH and are evaluated at all times during the whole integration. In all simulations with spin we set the dimensionless spin vector to $\vec{a} = (0.7, 0.7, 0)$, so we get maximum precession of the orbit of the star orbit lying in the X–Y plane.

The implementation of these relativistic terms follows the prescription given in the work of Kupa et al. (2006), which was the first work published about the inclusion of post-Newtonian corrections in the context of stellar dynamics. The addition of the spin to the problem was presented, also for the first time, in a stellar-dynamics context in Brem et al. (2013). Both, the periaapsis shift and the spin terms have been tested in detail, and partially published in the work of Brem et al. (2013) with a series of comparisons with the semi-Keplerian approximation of Peters (1964).

3 INITIAL CONDITIONS

In all simulations the mass of the MBH is $m_\bullet = 10^6 M_\odot$, the mass of the star is $m_\star = 1 M_\odot$ and it is set on an unbound, parabolic trajectory around the MBH, placed at the focus. It must be noted that while bound orbits are less “expensive” computationally, the most natural orbits are unbound ones, i.e. parabolic or hyperbolic, because we do not expect the region of phase-space close to the MBH to produce bound orbits, at least in a Milky Way-like galaxy (see e.g. Amaro-Seoane 2018; Baumgardt et al. 2018; Schödel et al. 2018; Gallego-Cano et al. 2018).

When the stars approach the MBH it will experience strong tidal forces whenever the work exerted over the star by the tidal force exceeds its own binding energy, (all energies are per unit mass), which is

$$E_{\text{bind}} = \frac{3 G m_\star}{(5-n)r_\star}, \quad (2)$$

where n is the polytropic index (Chandrasekhar 1942), m_\star the mass of the star. This allows us to introduce a typical radius for this to happen, the tidal radius r_t . Considering $r_\star \ll r_t$,

$$r_t = \left[\frac{(5-n)}{3} \frac{m_\bullet}{m_\star} \right]^{1/3} 2 r_\star. \quad (3)$$

With m_\bullet the mass of the MBH. For a solar-type star, considering an $n = 3$ polytrope, and $m_\bullet = 10^6 M_\odot$, we have that

$$r_t = 110 R_\odot \sim 0.51 \text{ AU}. \quad (4)$$

The initial distance of the star to the MBH is set to 20 times the axis of symmetry of the parabola, i.e. the pericentric distance between the MBH and the star. In order to investigate the fate of the bound material to the star and the fallback rate, we have chosen a series of trajectories with different penetration factors β , which is defined to be the ratio between the tidal radius and the distance of periaapsis, 1.5, 2, 3, 4, 5 and 9, and run for each case (i) a Newtonian simulation, (ii) a relativistic simulation taking into account only the periaapsis shift of the SPH particles and (iii) a relativistic simulation taking into account this effect and the spin correction.

It must be noted that the value for the penetration factors has been estimated by assuming a point-particle trajectory. However, in the relativistic cases, an initially assigned value for β diverges as the star progresses in its orbit towards the MBH as a function of the penetration factor. When the extended star achieves the vertex of the parabola, the penetration factor has differed from the initially chosen value. Hence, we initially set the star in that point-particle trajectory for those specific β values, and we derive the real penetration factor when it reaches the vertices of the relativistic cases. These are $\beta = 1.64, 2.26, 3.62, 5.15, 6.83$ and 12.05 , and we use them in the Newtonian cases as well so as to be able to compare the results. These values in turn correspond to the following distances of periaapsis: $r_{\text{peri}} \sim 0.32, 0.22, 0.14, 0.1, 0.07, 0.04 \text{ AU}$. For a parabolic orbit, the velocity of the star at periaapsis is $v_{\text{peri}} = \sqrt{2\mu/r_{\text{peri}}}$, with $\mu = Gm_\bullet \simeq 1.3 \times 10^{26} m^3 s^{-2}$, so that the corresponding velocities are $v_{\text{peri}} \sim 7.37 \times 10^7, 8.88 \times 10^7, 1.11 \times 10^8, 1.32 \times 10^8, 1.57 \times 10^8, 2.08 \times 10^8 \text{ m/s}$ which in units of the speed of light c are, respectively, $0.24, 0.29, 0.37, 0.44, 0.52, 0.69$.

The stars are modelled as main-sequence (MS) stars with a polytrope of index 3 constructed initially following the method of (Freitag & Benz 2005, in particular, see their on-line complements). We employ half a million particles to construct the polytrope, which is enough to solve the tidal disruption process. Enlarging this number by a number below at least an order of magnitude does not necessary lead to a significant improvement of the simulation (see section 3 of Rasio 2000).

4 QUANTITATIVE ANALYSIS

One important aspect in the process is the evolution of the star after the first periaapsis passage. To determine which part of the gas particles in the simulation is still bound or unbound to the star, we follow the following prescription (based in the work of Lai et al. 1993; Fulbright et al. 1995):

So as to decide whether a gas particle i is bound to the star, we calculate the specific energy of this particle relative to the star,

$$\epsilon_i = v_i + \frac{1}{2}v_{\text{rel}}^2 - \sum_j \frac{Gm_i m_j}{r_{ij}}, \quad (5)$$

where v_i and v_{rel} are respectively the internal energy and the relative velocity of gas particle i to the center of mass velocity of all the gas particles belonging to the star. The potential part is summed up over all star particles j . If $\epsilon_i > 0$, the particle is considered unbound from the star, otherwise bound. In the first step of the iteration, all particles are assumed to be star particles. After evaluating Eq. 5, particles are reassigned to be either still part of the star or unbound. In the next step, the specific energy is evaluated with respect to the reduced fraction of star particles. We stop the iteration when reassignments to the unbound component cannot be made. After the iteration is complete we check which part of the gas that is no longer gravitationally bound to the star is on Keplerian orbits around the MBH or completely unbound from the system. This part of the gas is then considered for the luminous fallback onto the MBH.

In Fig. (1) we show the fate of the material stripped (bound) from (to) the star for the different penetration factors mentioned before up to 3.62. The scaling of the first two panels in all these figures is the same in order to be able to compare better. In all figures we also add a third panel showing the long-term evolution of the Newtonian cases. We can see from these figures that the amount of bound mass to the star, i.e. the survival star, is in all cases larger in the relativistic simulations than in the Newtonian counterparts. For the relativistic cases, about 70%, 40%, 20% of the star survives the disruption after one day for the first three values of $\beta = 1.64, 2.26, 3.62$, while in the Newtonian simulations, this quantity is only about 50%, 5%, 2%. These results are general in agreement with the amount of mass of the survival core found by the work of Ryu et al. (2020c).

In Figure (2) we depict the same as in Fig. (1) for the two most extreme penetration factors, $\beta = 5.15, 12.05$ (this last penetration factor the star is still at a distance of two Schwarzschild radii from a Schwarzschild MBH of mass $10^6 M_\odot$). In this case, the amount of bound material to the star in the Newtonian cases further decreases as compared to larger β values. It is of about 1% and 0% respectively. However, the relativistic cases show a much larger survival stellar object, with a mass of about 38% for $\beta = 5.15$ and of about 42% for the most extreme case, $\beta = 12.05$; i.e. a larger quantity. In the relativistic simulations the amount of bound material to the star is larger than in their Newtonian counterparts, even at the smallest value of β .

In this first case, for $\beta = 1.64$, we observe in the Newtonian case of Fig.(1) that a significant amount of matter of the star survives the close interaction with the MBH. Indeed, Guillochon & Ramirez-Ruiz (2013) estimated that (Newtonian) TDEs have 100% disruption only for penetration factors $\beta > 1.85$. Recently, Miles et al. (2020) have studied (Newtonian) partial disruptions that corroborate the fallback rate proportion of $\propto t^{-9/4}$. Other scenarios, like the progressive disruption of a star as result of a tidal separation, however, lead to different eccentricities which predict a different scaling of $\propto t^{-1.2}$ Amaro-Seoane et al. (2012).

Also, Ryu et al. (2020c) find $\propto t^{-p}$ with $p \in [2, 5]$ depending on the mass of the star and the role of their relativistic implementation.

In Fig. (3) we show the last snapshot of the Newtonian simulation with $\beta = 1.64$ using the visualization tool of Price (2007) to render the gas particles. Embedded in the figure we have added a zoom of the area corresponding to what seems to be the remaining core of the star. However, this is a transient feature, as we can see in the uppermost, right panel of Fig. (1). We integrated the system for up to some ~ 18 days from the starting point, and we can see that the amount of mass decays very quickly with time, while the amount of matter of the original star bound to the MBH is kept constant. This episodic core will not be bound to the star at later times. However, it appears later as an enhanced fallback of debris in the first panel of Fig. (4) at later times, as we will explain in the next section.

5 FALLBACK RATE

So as to test the implementation of the orbit and the behavior of the SPH star, we calculate the fallback rate on to the MBH. For this, we calculate the required time for the bound debris to come back again to periaapsis by estimating the specific energy of each particle, $E = G(M + m)/(2a)$, with G the gravitational constant, M and m the masses of the MBH and one SPH particle, respectively.

From the angular momentum, one can derive that

$$e = \sqrt{1 + E \left(\frac{L}{\mu} \right)^2}, \quad (6)$$

where we have introduced $\mu = GM$ and neglect the contribution of m . If we define Δt as the ellapsed time between the first periaapsis passage and the current position of the particle's position, at a radius R from the MBH and time T , the necessary time for the next periaapsis passage is $t_{\text{peri}} = T - \Delta t$.

This distance is

$$R = a(1 - e \cdot \cos \epsilon), \quad (7)$$

with ϵ the eccentric anomaly; so that $\epsilon < \pi$ for outbound motion and $\epsilon > \pi$ for inbound motion. The mean anomaly can be calculated as

$$M = 2\pi \delta t / T = \epsilon - e \cdot \sin \epsilon, \quad (8)$$

and allows us to calculate the ellapsed time since the last periaapsis passage (at $M = 0$). We integrate the star's orbit until its center of mass has traveled far away from the tidal radius out to $3000R_\odot$, i.e. $\sim 12730 R_{\text{Schw}}$, with R_{Schw} the Schwarzschild radius of the MBH. From this point on we assume the gas particles to be traveling on independent, non-interacting Keplerian orbits solely determined by their orbital energy and angular momentum. From these values we compute the classical time until the subsequent pericenter passage, t_{peri} .

We present the results as fallback curves which are mass histograms over t_{peri} in Fig. (4) for different values of the

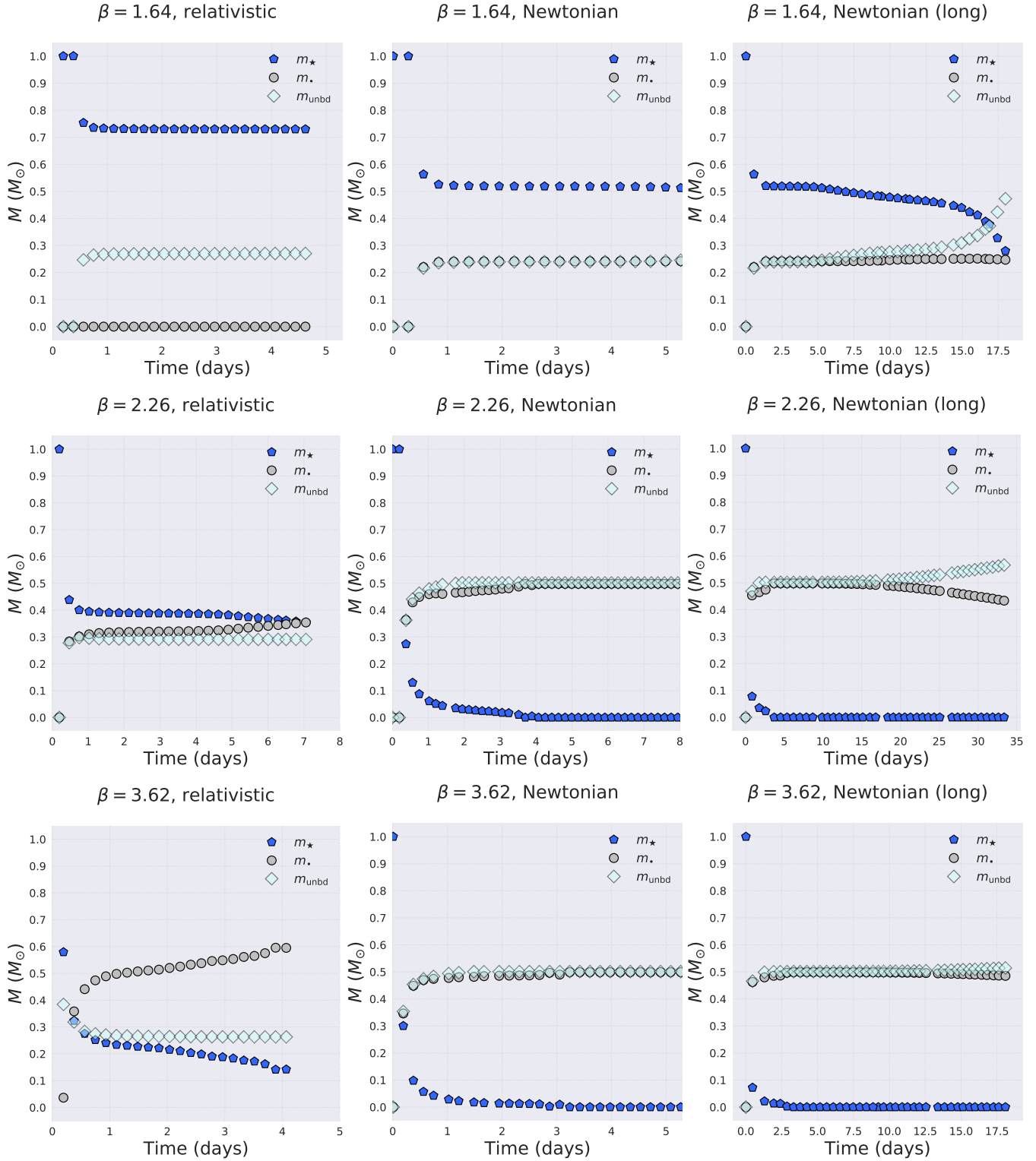


Figure 1. Amount of bound and ejected stellar mass for $\beta = 1.64$ as a function of time. In blue pentagons we depict bound stellar mass to the star, i.e. this represents the evolution of how much of the star remains after the TDE. In grey circles the amount bound to the MBH, and in cyan squares the unbound stellar mass, i.e. the mass of the star which is ejected. The left and middle panels correspond to the relativistic and Newtonian simulations set to the same limits, so as to be able to compare. The right panel is the Newtonian case integrated significantly further than in the left panel (labelled “long”).

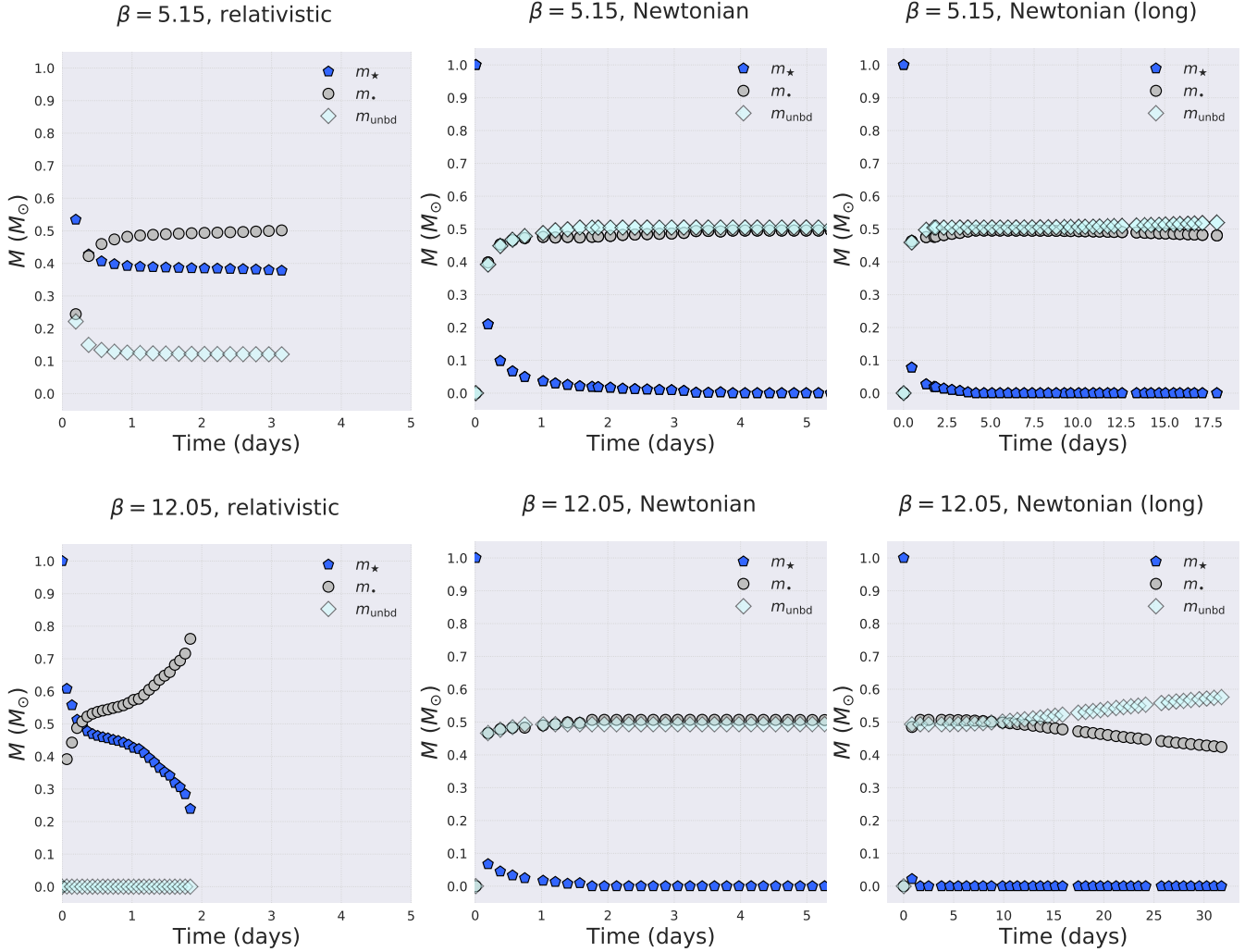


Figure 2. Same as Fig. (1) but for the two more extreme penetration factors, $\beta = 5.15$ and 12.05 .

penetration factor β . We can see that the lower value of β leads to a drop in the Newtonian fallback between 10^2 and 10^4 days, which can be envisaged as a result of matter falling back more quickly. This forms the depression around the later enhanced fallback. This is matter which is bound to the MBH, not to the original star, which has started to become bound to itself after the evolution. The relativistic cases also display this feature but at much earlier times and with much smaller depressions. This partial disruption leads to fallback values in the Newtonian case which are similar to the relativistic ones, as in the next value of $\beta = 2.26$. From that value upwards, the Newtonian cases lead to fallback values significantly higher than the relativistic ones, starting with about half an order of magnitude up to about five orders of magnitude for the deepest penetration and the spin case. We can observe only a clear effect of the spin when we go to extreme penetration values, the lowermost, right panel, with $\beta = 12.05$.

In Fig. (5) we show a mosaic with nine different snapshots in the evolution of the Newtonian case of $\beta = 2.26$. As we zoom in, we can see that at later times, 5.73 days, no surviving core is left. This situation changes completely when we consider the relativistic corrections, as we can see in

its counterpart, Fig. (6), which takes into account the post-Newtonian correcting terms. We can clearly see the survival of a core which is bound to the original star, as shown in Fig. (1).

This difference becomes even more evident when comparing the extreme case of $\beta = 12.05$, in Fig. (7), the Newtonian case and Fig. (8). Short after the passage through periaapsis, nothing is left from the original star in the Newtonian case, while in the relativistic one we find a surviving core at much later times.

6 AN EVALUATION OF THE ENERGY

In order to understand the outcome of the results, we evaluate the internal energy of the star in both the relativistic and Newtonian cases. For simplification, we approximate the star as a perfect fluid. The internal energy of a perfect fluid is given by the equation:

$$U = \frac{3}{2} N k_B T, \quad (9)$$

where N is the number of particles, k_B is the Boltzmann con-

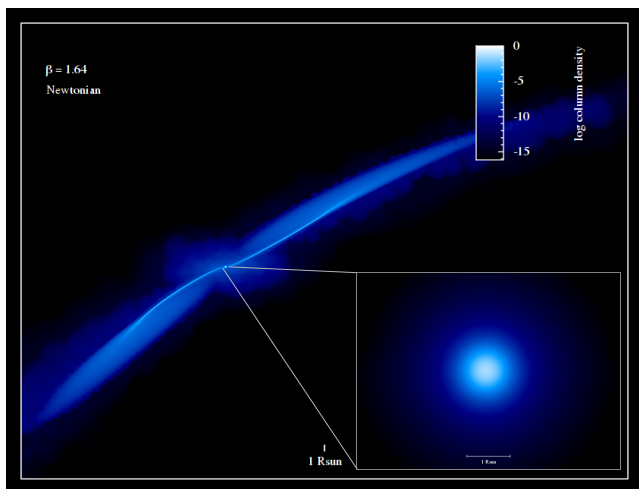


Figure 3. Last snapshot of the Newtonian simulation for $\beta = 1.64$. Both panels have a reference bar showing the length of a solar radius (“Rsun”) to set the scale. The bar depicting the logarithm of the column density of gas in the zoom has been set to the minimum and maximum values of -3.43 and 0 , respectively for a better identification of the structure.

stant, and T is the temperature. We can express N in terms of the mass of the star m_* and the mean molecular weight μ as $N = m_*/\mu$. The mean molecular weight is approximately $\mu \approx 1$ for a fully ionized gas, which is a reasonable approximation for the interior of a star. The temperature of the star can be approximated as $T \approx 10^7$ K, which is typical for the core of a main-sequence star.

In the Newtonian case, the gravitational potential energy of the star is given by:

$$U_{\text{Newt}} = -\frac{3Gm_*^2}{5r_*}, \quad (10)$$

where G is the gravitational constant, m_* is the mass of the star, and r_* is the radius of the star. This equation comes from the standard formula for the gravitational potential energy of a uniform sphere.

In the relativistic case, the gravitational potential energy of the star is modified by the presence of the black hole. The gravitational potential energy in the relativistic case can be approximated as:

$$U_{\text{Rel}} = -\frac{3Gm_*^2}{5r_*} \left(1 + \frac{3Gm_*}{2c^2 r_*} \right), \quad (11)$$

where c is the speed of light. The term $\frac{3Gm_*}{2c^2 r_*}$ is the post-Newtonian correction to the gravitational potential energy, which becomes significant when the star is close to the black hole (see e.g. Shapiro & Teukolsky 1983). We can then calculate the ratio of the internal energy in the relativistic case to the internal energy in the Newtonian case as:

$$\text{Ratio} = \frac{U_{\text{Rel}}}{U_{\text{Newt}}}. \quad (12)$$

Substituting the values for U_{Rel} and U_{Newt} into this equation, we find that the ratio is approximately 2.37×10^6 . This suggests that the internal energy of the star in the relativistic

case is about one million times larger than in the Newtonian case.

The large energy ratio indicates that the internal energy of the star is significantly higher in the relativistic case compared to the Newtonian case. This is primarily due to the additional energy contributions from the relativistic effects, such as the gravitational redshift and time dilation near the black hole, which are not present in the Newtonian case.

The implications for the star are significant. In the Newtonian case, the star’s internal energy is not sufficient to counteract the tidal forces from the black hole, leading to the star’s disruption. However, in the relativistic case, the higher internal energy could potentially allow the star to withstand the tidal forces to a greater extent. This could result in a larger portion of the star surviving the close encounter with the black hole.

7 GEODESIC CONVERGENCE OF PARTICLES ON A PARABOLIC ORBIT AROUND A SPINNING MASSIVE BLACK HOLE

One better way to try to understand why a core survives in the relativistic simulations is to calculate the geodesic convergence (or divergence) of the elements of the star as it approaches the pericentre of the MBH. Once we have the result for two test particles, we will extend the result to a group of them distributed in a spherical fashion and try to derive whether they build up a denser core in the relativistic case or not. I.e. we want to see whether the particles tend to get closer in the relativistic case of this “dust star” as compared to the Newtonian case. If this is the case, then we could understand the outcome of the SPH simulations. However, this is not an easy problem that involves several steps and concepts. Here is a list of the steps we would need to address to solve it.

We first need to calculate the geodesic deviation equation, which describes the relative acceleration of nearby geodesics in a curved spacetime. It can be used to calculate the separation between particles in the dust star. The equation is given by:

$$\frac{d^2 \xi^\alpha}{d\tau^2} = -R^\alpha_{\beta\mu\nu} u^\beta u^\mu \xi^\nu, \quad (13)$$

where $D/d\tau$ is the covariant derivative along the geodesic, ξ^α is the separation vector between the geodesics, u^α is the four-velocity of the particles, and $R^\alpha_{\beta\mu\nu}$ is the Riemann curvature tensor.

We will also need to estimate the tidal tensor, given by the projection of the Riemann tensor onto the observer’s local rest frame. It describes the tidal forces experienced by the dust star due to the black hole. In the Newtonian limit, the tidal tensor is given by the second spatial derivatives of the gravitational potential. In the relativistic case, it can be calculated from the geodesic deviation equation. The relativistic corrections to the Newtonian orbit can be calculated using the post-Newtonian approximation. The main corrections are due to the perihelion shift and the frame-dragging effect caused by the spin of the black hole. The perihelion shift can be calculated using

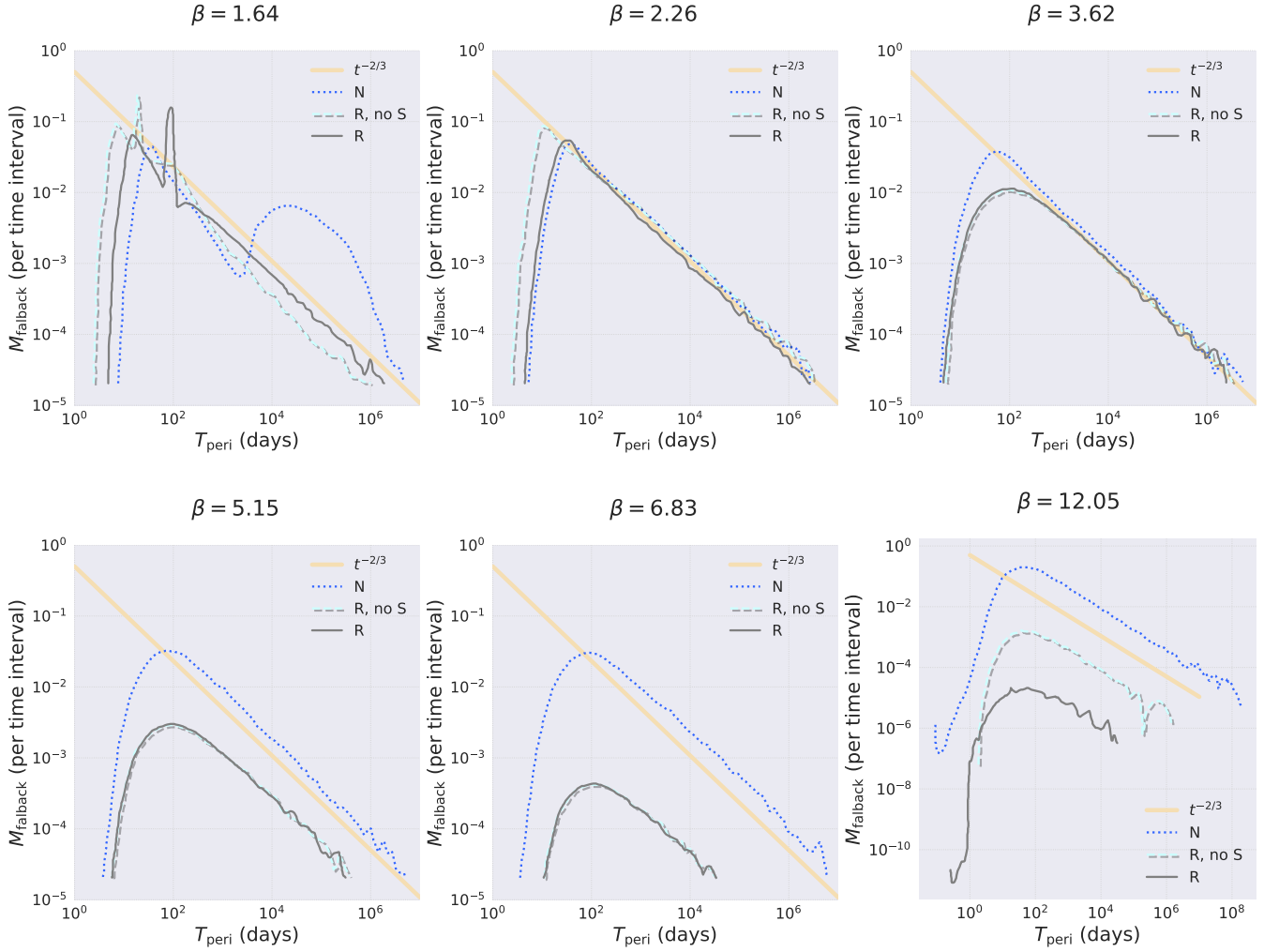


Figure 4. Fallback rate for a polytrope of index 3, mass $1 M_{\odot}$, radius $1 R_{\odot}$ and 500,000 particles. The curves delimit the upper part of histograms relative to the amount of bound stellar mass per time interval, distributed in intervals of T_{peri} , in days. The dotted, blue curve corresponds to the Newtonian (N) simulations, the long-dashed, grey curves to the relativistic cases without spin (R, no S) and the solid, grey curves to the relativistic runs taking into account spin corrections (R). The solid, light-orange line depicts the power-law described in the work of Rees in which the fallback rate is $\propto t^{-5/3}$. The reason for the exponent being $-2/3$ and not $-5/3$ is to correct for the logarithmic representation of the results, since the derivative of the mass M respect to the logarithm of time, t , $dM/d(\log(t)) \propto t \cdot dM/dt$. Hence, for a relation such as $dM/dt \propto t^{-x}$, $dM/d(\log(t)) \propto t^{-x+1}$, and so $-5/3 + 1 = -2/3$.

$$\Delta\varphi = 6\pi \frac{GM}{c^2 a(1 - e^2)}, \quad (14)$$

where G is the gravitational constant, M is the mass of the black hole, c is the speed of light, a is the semi-major axis of the orbit, and e is the eccentricity. The frame-dragging effect can be calculated using the Kerr metric, which describes the spacetime around a rotating black hole. The change in the density distribution of the dust star can be calculated by integrating the geodesic deviation equation over the volume of the star. This will give the change in volume, and hence the change in density, as a function of time.

7.1 Two test particles

The geodesic deviation equation describes the relative acceleration of nearby geodesics in a curved spacetime. It can be

used to calculate the separation between the two particles as they approach the pericentre. The equation is given by Eq. (13). In the case of a Schwarzschild black hole, the Riemann tensor has only one independent component, which can be written in terms of the mass M of the black hole and the radial coordinate r as:

$$R_{trtr} = -\frac{2GM}{c^2 r^3}. \quad (15)$$

The geodesic deviation equation then simplifies to:

$$\frac{d^2 \xi^r}{d\tau^2} = -R_{trtr} u^t u^t \xi^r = \frac{2GM}{c^2 r^3} (u^t)^2 \xi^r, \quad (16)$$

where ξ^r is the radial component of the separation vector, and u^t is the time component of the four-velocity. Assuming that the two particles are initially at rest with respect to each other, we have $\xi^r = D$ and $u^t = dt/d\tau$, where t is the

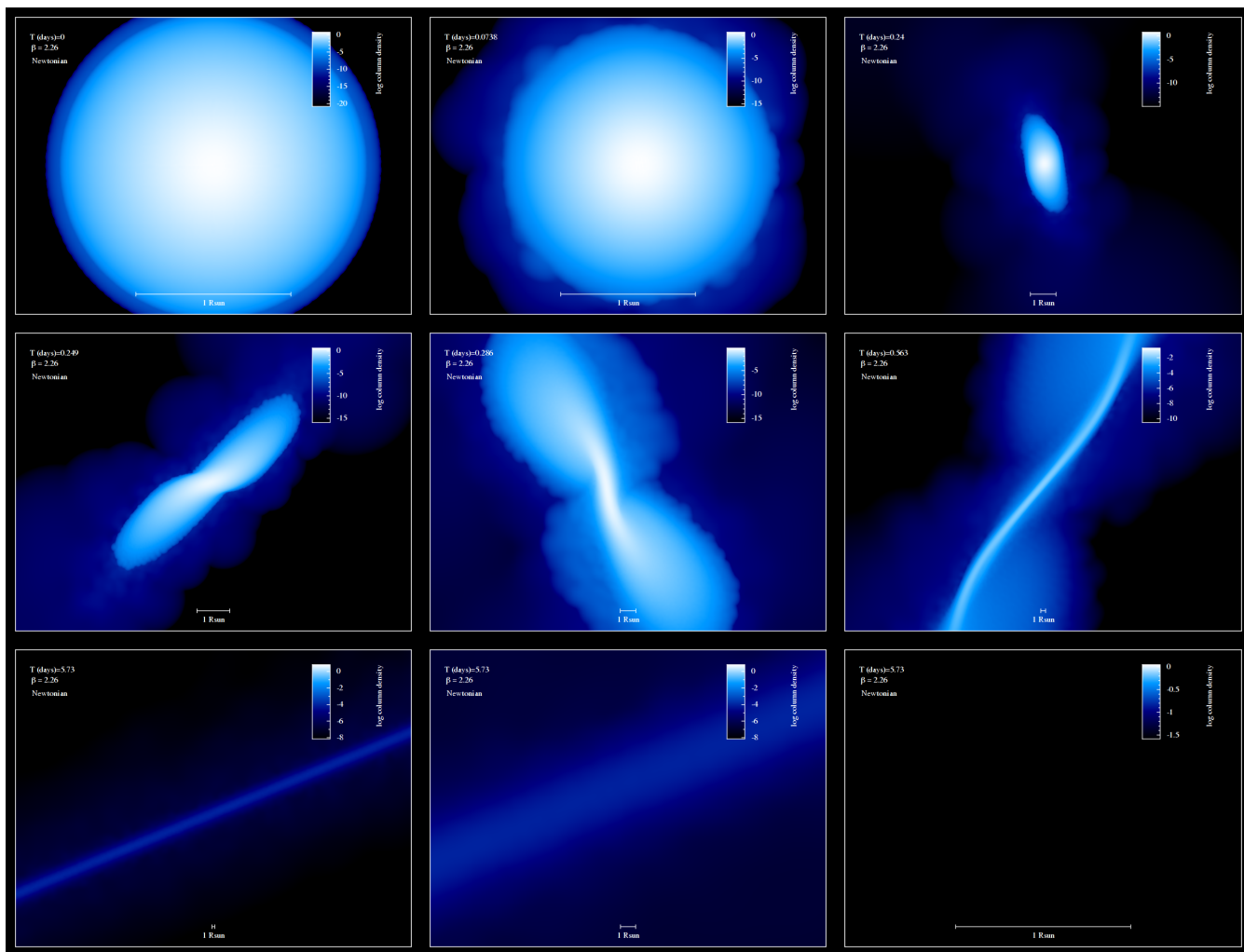


Figure 5. Mosaic of different instants of time corresponding to the Newtonian simulation of penetration factor $\beta = 2.26$. From the top to the bottom, left to right, we show six different moments in the evolution of the star in its reference frame, more specifically at (approximately) $T = 0, 0.07, 0.24, 0.29, 0.56$ and 5.73 days. As a reference point, we show the length corresponding to one solar radius in each panel, and the (logarithm) of the column density of the star at top on the right. Both the zoom factor and the depth of the logarithmic scale in the column density have been chosen in each frame to show the most interesting features, and they do not necessarily match from frame to frame. The last three panels depict the last moment, 5.73 days, at different zoom levels of the densest region. The last one shows an empty area because the depth of the column density is set to values not found.

coordinate time and τ is the proper time. The equation then becomes:

$$\frac{d^2 D}{dt^2} = \frac{2GM}{c^2 r^3} \left(\frac{dt}{d\tau} \right)^2 D. \quad (17)$$

This is a second-order differential equation for D as a function of t . The solution will depend on the initial conditions, which are given by $D(0) = D_0$ and $D'(0) = 0$, where D_0 is the initial separation between the particles. The solution to this equation will give the separation D between the particles as a function of time as they approach the pericentre. The value of D at the pericentre can then be obtained by evaluating the solution at the time of pericentre passage.

Also, the spin of the black hole introduces an additional term in the geodesic deviation equation, which accounts for the frame-dragging effect. This effect is caused by the rotation of the black hole, which drags the surrounding space-

time along with it. The geodesic deviation equation in the presence of a rotating black hole (Kerr black hole) in Fermi normal coordinates is given by:

$$\frac{d^2 D^i}{dt^2} = -R^i{}_{0j0} D^j - 2v^k \Omega_{kj} D^j, \quad (18)$$

where v^k is the velocity of the test particle, Ω_{kj} is the angular velocity of the frame-dragging effect, and the other symbols have the same meaning as before.

The second term on the right-hand side represents the effect of the black hole's spin. This term causes a precession of the test particles' orbits, which can lead to an increase in the separation between the particles, and hence an increase in the density of the dust star.

However, solving this equation analytically to find the separation $D(t)$ as a function of time in the presence of a spinning black hole is a complex task that would typically

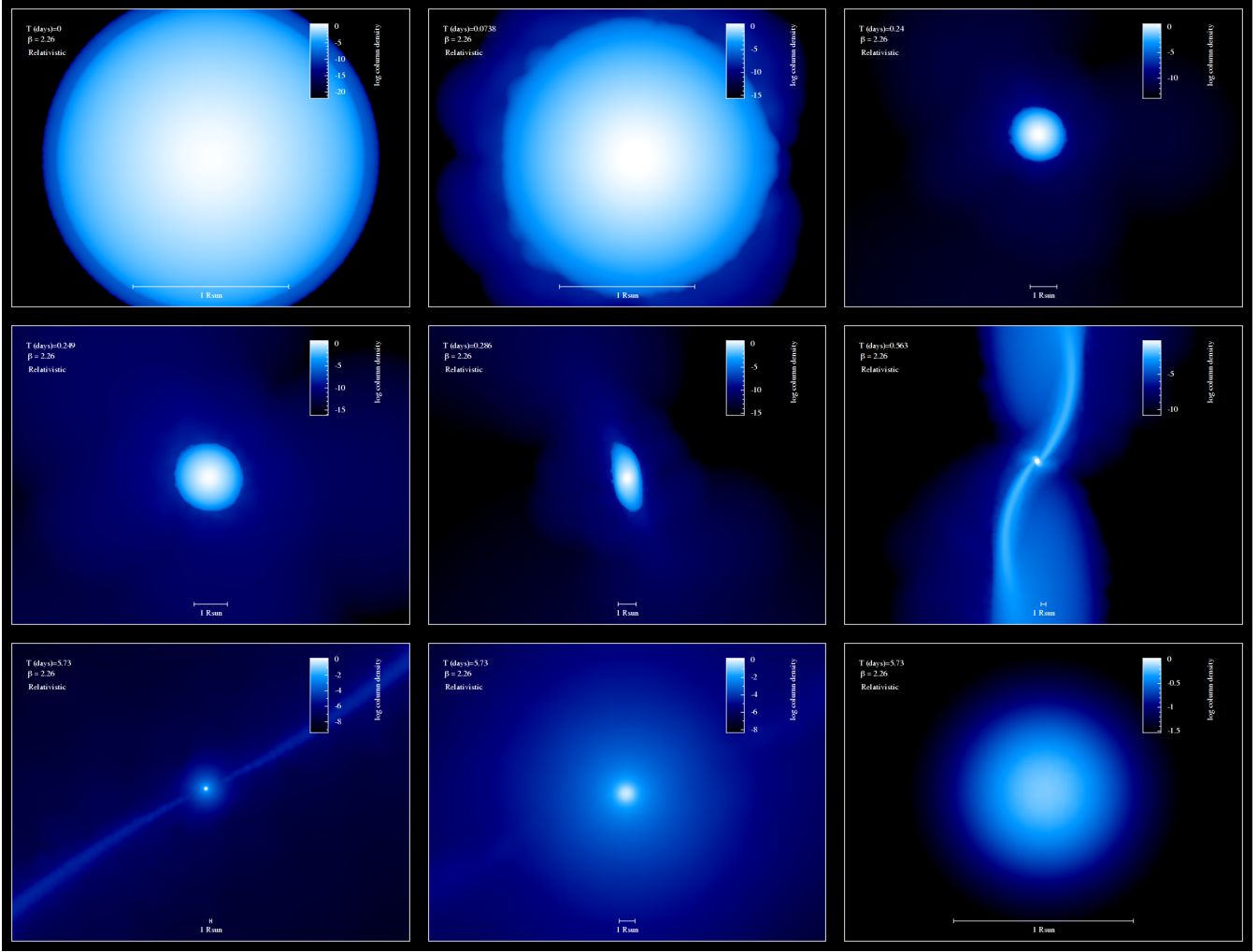


Figure 6. Same as Fig. (5) for the relativistic counterpart. Whilst in the previous figure the last panels show a thread-like distribution of the gas debris, in the relativistic counterpart we see a survival core with a size of about half of the initial star. Both, the lengths and the density of the gas have been set to almost identical values to those shown in Fig. (5), so as to be able to compare panel by panel of both figures.

requires numerical methods. To simplify the problem, we can make a few approximations. We will assume that the gravitational field of the black hole is weak at the location of the particles. This is valid if the particles are far from the event horizon of the black hole. Also, we will assume that the particles are moving slowly compared to the speed of light. This is valid if the kinetic energy of the particles is much less than their rest mass energy. The Fermi normal coordinates are a local coordinate system in which the metric of spacetime is approximately Minkowskian. They are particularly useful for calculating the tidal forces experienced by a small body moving in a curved spacetime.

The Riemann tensor in Fermi normal coordinates can be calculated from the metric. The only non-zero component is:

$$R_{trtr} = -\frac{2GM}{c^2 r^3}. \quad (19)$$

The geodesic deviation equation then becomes:

$$\frac{d^2 \xi^r}{d\tau^2} = -R_{trtr} u^t u^t \xi^r = \frac{2GM}{c^2 r^3} (u^t)^2 \xi^r. \quad (20)$$

where ξ^r is the radial component of the separation vector, and u^t is the time component of the four-velocity. Assuming that the two particles are initially at rest with respect to each other, we have $\xi^r = D$ and $u^t = dt/d\tau$, where t is the coordinate time and τ is the proper time. The equation then becomes:

$$\frac{d^2 D}{dt^2} = \frac{2GM}{c^2 r^3} \left(\frac{dt}{d\tau} \right)^2 D. \quad (21)$$

This is a second-order differential equation for D as a function of t . The solution will depend on the initial conditions, which are given by $D(0) = D_0$ and $D'(0) = 0$, where D_0 is the initial separation between the particles. I.e. we are simplifying the problem by assuming that initially the particles have a relative velocity of zero, so as to be able to assess the evolution of the system once it reaches pericentre.

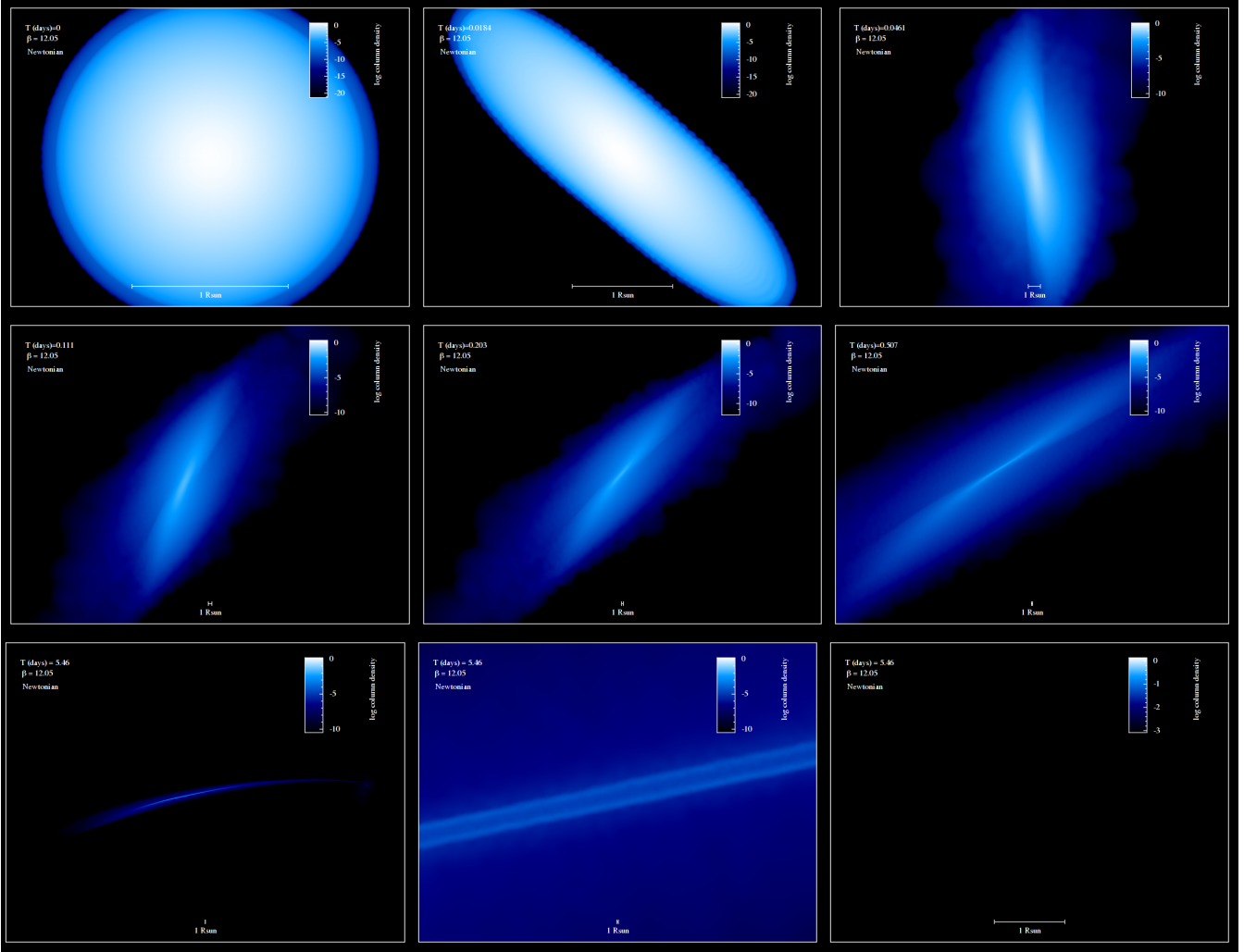


Figure 7. Same as in Fig. (5) but for a value of $\beta = 12.05$ and different times of the total integration. The last panel again shows nothing because the scale of the column density of the star is set to the same values of Fig. (8), which we have chosen to show the survival core of the star. In this Newtonian case, however, the gas density is so low that nothing appears.

The solution to this equation will give the separation D between the particles as a function of time as they approach the pericentre. The value of D at the pericentre can then be obtained by evaluating the solution at the time of pericentre passage. In the case of a Kerr black hole, the spacetime is not only curved due to the mass of the black hole, but also twisted due to its spin. This leads to an additional effect known as frame-dragging, which can affect the motion of the test particles.

In the weak field and slow motion approximations, the geodesic deviation equation in the equatorial plane ($\theta = \pi/2$) of a Kerr black hole in Fermi normal coordinates is given by:

$$\frac{d^2 \xi^r}{dt^2} = \frac{2GM}{c^2 r^3} \left(\frac{dt}{d\tau} \right)^2 \xi^r - \frac{4GJ}{c^2 r^3} \left(\frac{dt}{d\tau} \right) \xi^\phi, \quad (22)$$

where ξ^ϕ is the azimuthal component of the separation vector, and $J = aGM/c$ is the angular momentum of the black hole, with a being the spin parameter. This equation describes the radial tidal force experienced by the test particles,

as well as the frame-dragging effect due to the spin of the black hole. The second term on the right-hand side is the frame-dragging term, which is proportional to the spin parameter.

Assuming that the two particles are initially at rest with respect to each other, we have $\xi^r = D$ and $\xi^\phi = 0$, and $u^t = dt/d\tau$, where t is the coordinate time and τ is the proper time. The equation then becomes:

$$\frac{d^2 D}{dt^2} = \frac{2GM}{c^2 r^3} \left(\frac{dt}{d\tau} \right)^2 D. \quad (23)$$

This is a simple harmonic oscillator equation, and its solution is:

$$D(t) = D_0 \cos \left(\sqrt{\frac{2GM}{r^3}} t \right), \quad (24)$$

where D_0 is the initial separation between the particles.

As the particles approach the pericentre, the radial coordinate r decreases, and the frequency of the oscillation

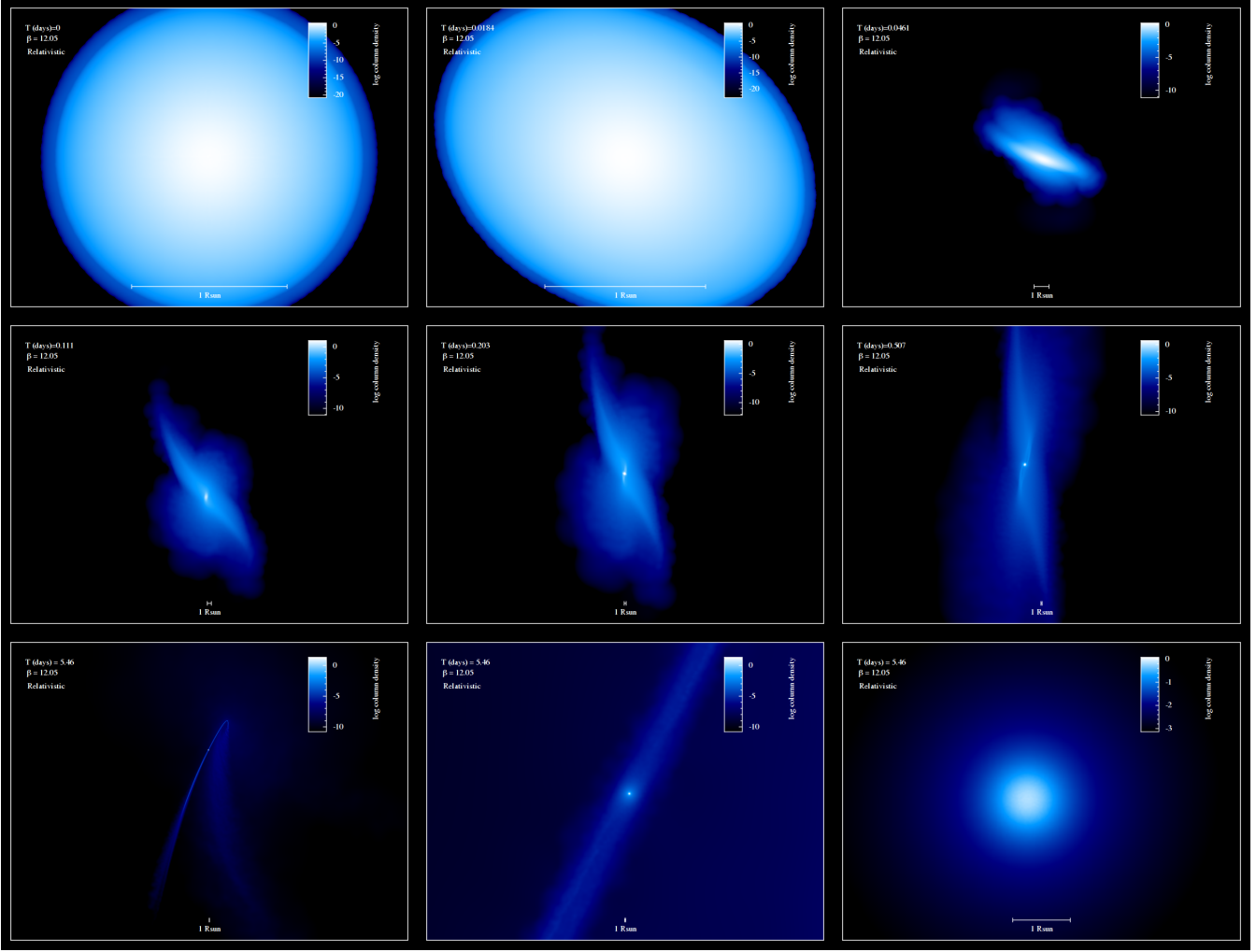


Figure 8. Same as Fig. (7) for the relativistic counterpart. Already at early times, the star in the relativistic cases suffers a less significant spread in size. Also in this case, a survival core is found clearly in the simulation.

increases. Therefore, the separation D between the particles oscillates with an increasing frequency, and its amplitude decreases. At the pericentre, the radial coordinate r is equal to the pericentre distance r_p , and the separation D is:

$$D(t_p) = D_0 \cos \left(\sqrt{\frac{2GM}{r_p^3}} t_p \right), \quad (25)$$

where t_p is the time of pericentre passage. Hence, under the weak field and slow motion approximations. It shows that the separation between the particles decreases as they approach the pericentre.

These equations show that the separation between the particles decreases as they approach the pericentre. This is consistent with the expectation that the particles should be drawn closer together by the gravitational pull of the black hole. The equations also show that the frequency of the oscillation of the separation increases as the particles approach the pericentre. This is due to the increasing strength of the gravitational field of the black hole.

7.2 A dust star

Expanding this estimation to a group of N test particles is a bit more complex, but the general idea is the same. Each pair of particles will experience a tidal force that tends to decrease their separation as they approach the pericentre.

Let us denote the initial separation between the i -th and j -th particles as D_{ij} . According to the previous analysis, the separation $D_{ij}(t)$ at time t is given by:

$$D_{ij}(t) = D_{ij,0} \cos \left(\sqrt{\frac{2GM}{r^3}} t \right), \quad (26)$$

where $D_{ij,0}$ is the initial separation between the i -th and j -th particles. The average separation $\bar{D}(t)$ between the particles at time t can be calculated as the average of $D_{ij}(t)$ over all pairs of particles:

$$\bar{D}(t) = \frac{1}{N(N-1)/2} \sum_{i < j} D_{ij}(t). \quad (27)$$

This is the average separation between the particles as a

function of time as they approach the pericentre. The value of $\bar{D}(t)$ at the pericentre can then be obtained by evaluating the above expression at the time of pericentre passage. The density $\rho(t)$ of the dust star at time t is inversely proportional to the cube of the average separation:

$$\rho(t) = \frac{M_{\text{star}}}{\bar{D}(t)^3}, \quad (28)$$

where M_{star} is the total mass of the dust star.

This suggests that the density of the dust star increases as the particles approach the pericentre, due to the tidal forces exerted by the black hole. However, this is an approximate result, and a more accurate calculation would require taking into account the specific distribution of particles in the dust star and solving the full geodesic deviation equation for each pair of particles.

In the Newtonian case, the geodesic deviation equation simplifies to:

$$\frac{d^2 D}{dt^2} = -\frac{GM}{r^3} D, \quad (29)$$

where D is the separation between the particles, t is the time, G is the gravitational constant, M is the mass of the black hole, and r is the radial coordinate. This is a simple harmonic oscillator equation, and its solution is:

$$D(t) = D_0 \cos\left(\sqrt{\frac{GM}{r^3}} t\right), \quad (30)$$

where D_0 is the initial separation between the particles. At the pericentre, the radial coordinate r is equal to the pericentre distance r_p , and the separation D is:

$$D(t_p) = D_0 \cos\left(\sqrt{\frac{GM}{r_p^3}} t_p\right), \quad (31)$$

where t_p is the time of pericentre passage.

The difference between the separation at the pericentre and the initial separation is:

$$D(t_p) - D_0 = D_0 \left| \cos\left(\sqrt{\frac{GM}{r_p^3}} t_p\right) - 1 \right|. \quad (32)$$

This difference is virtually zero for any choice of the initial separation D_0 , because the cosine function oscillates between -1 and 1. This means that the separation between the particles does not change significantly in the Newtonian case and hence there is not a density peak developing, as in the relativistic case.

7.3 The role of hydrodynamics

We have seen that in the relativistic case, the gravitational force is modified by corrections that become more significant as the particles approach the black hole. These corrections include terms that depend on the speed of the particles, which becomes larger as they get closer to the black hole. If these particles were part of a star in a stellar interior, the frame-dragging effect would help to stabilize the rotation

of the star, while the Lense-Thirring effect would cause a precession in the orientation of the star's orbit around the center of mass. These effects would help to provide additional stability to the structure of the star.

One could however argue that this is an approximation only valid for a fictitious star made out of “dust” particles, and not representative of a real star, where hydrodynamical phenomena might change the outcome. We will argue now that the test particle approach is fine for this study.

To calculate the time spent by the particles in the regime where 1PN and 1.5PN post-Newtonian corrections dominate the evolution, we need to find the time at which the Newtonian acceleration becomes of the same order as the 1PN and 1.5PN corrections. At leading order, the Newtonian acceleration is given by

$$a_N = -\frac{GM}{r^2}, \quad (33)$$

where r is the distance between the particles and M is the mass of the central black hole. The 1PN correction to the acceleration is given by (Will 2018)

$$a_{1PN} = -\frac{GM}{r^2} \left(\frac{3v^2}{c^2} + 2 \right), \quad (34)$$

and the 1.5PN correction is given by (Will 2018)

$$a_{1.5PN} = \frac{2G^2 M^2}{r^4 c^4} (4v^4 + 12v^2 c^2 - 3c^4). \quad (35)$$

To find the associated timescale, we will use the distance between the particles as r . Therefore, the acceleration at leading order becomes $a_N = -GM/(0.3R_\odot)^2$, for an illustrative initial separation of $0.3R_\odot$. At the point where the 1PN and 1.5PN corrections are of the same order as a_N , we can write

$$a_{1PN} = a_{1.5PN} = \alpha \frac{GM}{(0.3R_\odot)^2}, \quad (36)$$

where α is a dimensionless constant that depends on the velocity of the particles. Solving for r , we find

$$r = \frac{\alpha^{1/2}}{2^{1/6}} \left(\frac{5GM}{3c^2} \right)^{1/3}. \quad (37)$$

The time spent by the particles in the regime where post-Newtonian corrections dominate can be found by dividing the distance in Eq. (37) by the velocity of the particles, v . Since we are interested in the time it takes for the particles to reach periapsis, we can use the initial separation between the particles, $0.3R_\odot$, as an estimate for the velocity. Therefore, the timescale is given in seconds by

$$t_{\text{scale}} = \frac{r}{0.3R_\odot} \text{ s}. \quad (38)$$

We note that this is the time it takes for the particles to reach periapsis assuming that they are moving at constant velocity. In reality they are not, because they are approaching the periapsis and will be accelerating. Therefore, we are being conservative about the estimate; in practise the time

will be even shorter but we can envisage this as an upper limit.

The hydrodynamical timescale is given by $\tau_{\text{hydro}} \sim \sqrt{R_*^3/(Gm_*)}$, where R_* is the radius of the star and m_* is its mass. For a solar-type star, this timescale is on the order of $\tau_{\text{hydro}} \sim 1600$ seconds. Comparing this timescale to the time spent in the regime where the 1PN and 1.5PN corrections dominate, we can determine if the hydrodynamical effects can be neglected during this time. The time spent in this regime can be calculated by finding the time it takes for the terms involving these corrections to become comparable to the Newtonian term. We can write this time as:

$$t_{\text{PN}} = \frac{\gamma}{c^3} \frac{X^4 r_p^4}{GM} \left[\frac{3}{2} + \frac{7}{2} \cos(2\phi) \right], \quad (39)$$

where m is the mass of the test particle, D is the initial separation of the test particles, and ϕ is the angle between the initial separation vector and the spin vector of the black hole. To simplify the notation, we have defined the dimensionless parameter $\gamma \equiv (11/8)(M/m)^{1/2}$, and we have chosen a fraction X of the pericentre distance r_p , such that $D = Xr_p$. To determine the maximum time spent in the post-Newtonian regime, we need to find the maximum value of Eq. (39) with respect to ϕ . This occurs when $\cos(2\phi) = 1$, so we obtain:

$$t_{\text{PN,max}} = \frac{1}{c^3} \frac{X^4 r_p^4}{GM} \gamma \frac{5}{2} \quad (40)$$

Using the values we calculated earlier for r_p and γ , we can evaluate the time spent by the particles in the regime where the 1PN and 1.5PN post-Newtonian corrections become significant. From Eq. (39) and following Peters & Mathews (1963), the total amount of time spent in this regime is

$$T_{\text{PN}} = \frac{5c^5 r_p^4}{256G^2 M^2 (1-e^2)^{7/2}} \left(2 + 2e^2 + \frac{9}{4}(1+3e^2)\gamma \right. \\ \left. - 3(1+e^2)\beta - \frac{39}{8}(1+3e^2)\gamma^2 - \frac{3}{2}(1-e^2)\beta^2 \right). \quad (41)$$

Substituting the values we obtained earlier for r_p and γ , we get:

$$T_{\text{PN}} = 3.72 \times 10^{-4} \left(\frac{M_\odot}{M} \right)^2 \text{ s}. \quad (42)$$

This is much shorter than the hydrodynamical timescale of a typical star, which is on the order of millions to billions of years, depending on the star's mass and evolutionary stage (Cox 1980). Therefore, we can safely neglect all hydrodynamical effects during the time in which the post-Newtonian forces dominate.

However, we also need to consider the timescale for the star to readjust to a perturbation caused by the gravitational interaction with the black hole. This timescale is determined by the star's sound-crossing time, which is the time it takes for a sound wave to travel across the star's diameter. For a typical main-sequence star with a radius of $R_\odot \approx 6.96 \times 10^8$ m and a sound speed of $c_s \approx 10^5$ m/s, the sound-crossing time is on the order of a few minutes. Therefore, we need to ensure that the timescale for the gravitational interaction

with the black hole is longer than the star's sound-crossing time. For the specific example we have been considering, with $M = 10^6 M_\odot$ and $r_p = 2.84 R_\odot$, we can calculate the ratio of the post-Newtonian timescale to the sound-crossing time as:

$$\frac{T_{\text{PN}}}{t_{\text{sc}}} \approx 3.7 \times 10^{-8}, \quad (43)$$

where t_{sc} is the sound-crossing time of the star. This confirms that we can neglect hydrodynamical effects during the post-Newtonian regime.

MORE REALISTIC STARS

Even if we just explained why conceptually it is fine to drop hydrodynamical effects in our “dust star” thought experiment, let us try to understand what a more realistic star would experiment so that we gain a bit more of intuition about the tidal disruption allowing a core to survive. Let us start with the Tolman-Oppenheimer-Volkoff (TOV) equation for hydrostatic equilibrium in the Newtonian approximation (see e.g. Kippenhahn & Weigert 1994),

$$\frac{dp}{dr} = -\frac{(p+\rho)(m+4\pi r^3 p)}{r(r-2m)}, \quad (44)$$

where p is the pressure, ρ is the density, m is the mass enclosed within a radius r , and r is the radial distance from the center of the star. To make the calculations simpler, we will consider a homogeneous star, a gas blob, so that the mass enclosed within a radius r is given by $m(r) = \frac{4}{3}\pi r^3 \rho$. This equation describes the balance between the gravitational force and the pressure gradient inside the star. In the Newtonian case, the gravitational force is balanced by the pressure gradient, which prevents the star from collapsing under its own weight.

Let us now include the 1PN and 1.5PN corrections to the TOV equation and solve it to find the evolution of the density as the star approaches the pericentre. The 1PN correction to the TOV equation is given by (again, see Kippenhahn & Weigert 1994):

$$\frac{dp}{dr} = -\frac{(p+\rho)(m+4\pi r^3 p)}{r(r-2m)} - \frac{4\pi r^2 (9p+5\rho+\rho \frac{dp}{dr}/p)}{r-2m}. \quad (45)$$

This equation includes the additional pressure gradient due to the relativistic correction to the gravitational force. The term $\rho \frac{dp}{dr}/p$ represents the change in density with respect to pressure. Next, we need to include the 1.5PN correction to the TOV equation. The 1.5PN correction accounts for the effect of the black hole's spin on the gravitational force, and is

$$\frac{dp}{dr} = -\frac{(p+\rho)(m+4\pi r^3 p)}{r(r-2m)} - \frac{4\pi r^2 (9p+5\rho+\rho \frac{dp}{dr}/p)}{r-2m} + \frac{4\pi r^2 (p+\rho)^2}{r-2m}. \quad (46)$$

This equation includes the additional pressure gradient due

to the relativistic correction to the gravitational force, including the effect of the black hole’s spin. The term $(p + \rho)^2$ represents the square of the total energy density in the star.

In order to derive the solution to find the evolution of the density as the star approaches the pericentre, we need to find a solution to this system. Even if we use a linear approximation for $\rho(r)$, i.e. we assume that the change in density is not large, the TOV equation with PN corrections is a non-linear differential equation which is not straightforward to solve analytically. However, we can still gain some insight from the form of the equation. The additional term, which is proportional to $(p + \rho)^2$, suggests that the pressure and density inside the star increase due to the relativistic effects. This is consistent with our earlier discussion that the gravitational force increases as the star approaches the black hole, and the pressure gradient must also increase to maintain hydrostatic equilibrium.

8 CONCLUSIONS

In this work we have addressed the problem of TDEs being less luminous than theoretically expected in the accretion disk model. We run a set of Newtonian SPH simulations of an unbound star of one solar mass and a MBH of mass $10^6 M_\odot$ with penetration parameters ranging from 1.64 to 12.05. We re-do the simulations with exactly the same β parameters and initial conditions but taking into account relativistic (post-Newtonian) corrections. For this we consider two different sets of simulations - One which only includes the first correction to periastris shift in the equations of motion and another which additionally takes into account the spin-orbit coupling correction up to next-to-lowest order. For β values starting at $\beta \gtrsim 2.25$, all relativistic simulations feature a surviving core of the original star. The Newtonian simulations, however, do not. Only the lowest value of $\beta = 1.64$ in the Newtonian case displays a core which does not last long bound to the original star. As a consequence, the fallback rates are lower in the corresponding relativistic cases, and hence the luminosity is also lower. The deeper the TDE, the bigger the difference in luminosity between the Newtonian and relativistic simulations. The effect of the spin only plays an important role, as expected, for extremely deep penetration factors. This was also noted by the work of Gafton & Rosswog (2019), who find that precession leads to debris configurations which are absent in the Newtonian cases.

Moreover, in the relativistic cases the energy distribution is more spread out, so that in each specific energy bin there is less matter. Hence, the fall back rate in every time step is lower; dM/dt is closely related to dM/dE , with E the specific energy relative to the MBH. This can be seen in e.g. Fig. 3 of Evans & Kochanek (1989) and the work of Ryu et al. (2020a,b), which shows that TDEs in the relativistic case has an energy distribution with significant wings, as well as Fig. 2 of Ryu et al. (2020c) and Ryu et al. (2020d) for a full disruption. If E is wider, dM/dE will be smaller and, thus, dM/dt as well.

The analysis has been primarily numerical but complemented by an analytical investigation. For this, we examine the energy dynamics and the behavior of geodesics in the context of a star approaching a black hole. We considered

the distance between two geodesics, which represents the tidal deformation experienced by the star as it approaches the black hole. We find that this distance decreases as the star gets closer to the black hole, indicating that the star is being stretched by the tidal forces. This stretching effect is a key factor in the tidal disruption of the star. We then extended our two-test particle analysis to a “dust star”, a simplified model of a star in which the particles move along geodesics and there are no internal forces. We found that the distance between the particles decreases as they approach the black hole, confirming the stretching effect observed in the geodesic analysis. However, we also found that this distance remains finite, indicating that the star does not get completely disrupted but retains a core.

An important question in this dust star approach is what role plays hydrodynamics. For this, we first calculate the time spent in the interesting regime; i.e. when the relativistic effects are important. We found that these corrections become significant at a certain distance from the black hole, which we calculated using the Newtonian acceleration as a reference. We then considered the timescale for the star to traverse this regime, which we found to be much shorter than the hydrodynamical timescale of a typical star. We then considered the timescale for the star to readjust to a perturbation caused by the gravitational interaction with the black hole. This timescale is determined by the star’s sound-crossing time, which is on the order of a few minutes for a typical main-sequence star. We found that the timescale for the gravitational interaction with the black hole is much shorter than the star’s sound-crossing time, confirming that we can neglect hydrodynamical effects during the post-Newtonian regime.

Finally, we considered the effects of the black hole’s gravity on the internal structure of the star, using the Tolman-Oppenheimer-Volkoff (TOV) equation for hydrostatic equilibrium. We included the 1PN and 1.5PN corrections to the TOV equation and found that the pressure and density inside the star increase due to the relativistic effects. Our analytical findings confirm the numerical results.

Our results suggest that in Nature TDEs must have deeper penetration parameters than previously thought to explain the observations. These orbits naturally lead to the consequence of a reduced observed luminosity regardless of the accretion disc, simply due to the fact that relativity allows a part of the star to survive the disruption. Future work should aim to solve the shocks that occur during this process, in order to better understand the non-thermal implications with the interstellar medium.

ACKNOWLEDGMENTS

The initial idea of this work was presented as a talk at the Alájar meeting in 2013¹ and later also as an invited talk at the workshop “TDE17: Piercing the sphere of influence”² which took place in Cambridge. PAS thanks the participants and organisers for encouraging him to publish the research and Enrico Ramírez-Ruiz, Pablo Laguna, Zoltan Haiman,

¹ <http://astro-gr.org/alajar-meeting-2013-stellar-dynamics-growth-massive-black-holes/>

² <https://www.ast.cam.ac.uk/meetings/2017/tde17.piercing.sphere.influence>

Julian Krolik, Nick Stone, Sterl Phinney, Ramesh Narayan, and Stephan Rosswog for comments during the workshop. He is particularly indebted to Julian Krolik for pointing him the publications by him and his collaborators.

We acknowledge the funds from the “European Union NextGenerationEU/PRTR”, Programa de Planes Complementarios I+D+I (ref. ASFAE/2022/014).

DATA AVAILABILITY

Any data used in this analysis are available on reasonable request from the first author.

REFERENCES

- Amaro-Seoane P., 2018, *Living Reviews in Relativity*, 21, 4
- Amaro-Seoane P., Miller M. C., Kennedy G. F., 2012, *MNRAS*, 425, 2401
- Arcavi I., Gal-Yam A., Sullivan M., Pan Y.-C., Cenko S. B., Horesh A., Ofek E. O., De Cia A., Yan L., Yang C.-W., Howell D. A., Tal D., Kulkarni S. R., Tendulkar S. P., Tang S., Xu D., Sternberg A., Cohen J. G., Bloom J. S., Nugent P. E., Kasliwal M. M., Perley D. A., Quimby R. M., Miller A. A., Theissen C. A., Laher R. R., 2014, *ApJ*, 793, 38
- Baumgardt H., Amaro-Seoane P., Schödel R., 2018, *A&A*, 609, A28
- Blanchet L., Iyer B. R., 2003, *Classical and Quantum Gravity*, 20, 755
- Brem P., Amaro-Seoane P., Spurzem R., 2013, *MNRAS*, 434, 2999
- Brenneman L., 2013, *Measuring the Angular Momentum of Supermassive Black Holes*
- Carter B., Luminet J. P., 1982, *Nat*, 296, 211
- , 1983, *A&A*, 121, 97
- Chandrasekhar S., 1942, *Physical Sciences Data*
- Chornock R., Berger E., Gezari S., Zauderer B. A., Rest A., Chomiuk L., Kamble A., Soderberg A. M., Czekala I., Dittmann J., Drout M., Foley R. J., Fong W., Huber M. E., Kirshner R. P., Lawrence A., Lunnan R., Marion G. H., Narayan G., Riess A. G., Roth K. C., Sanders N. E., Scolnic D., Smartt S. J., Smith K., Stubbs C. W., Tonry J. L., Burgett W. S., Chambers K. C., Flewelling H., Ho-dapp K. W., Kaiser N., Magnier E. A., Martin D. C., Neill J. D., Price P. A., Wainscoat R., 2014, *ApJ*, 780, 44
- Cox J. P., 1980, *Principles of Stellar Structure*. Gordon and Breach Science Publishers
- Evans C. R., Kochanek C. S., 1989, *ApJ Lett.*, 346, L13
- Faye G., Blanchet L., Buonanno A., 2006, *Ph. Rv. D.*, 74, 104033
- Frank J., Rees M. J., 1976, *MNRAS*, 176, 633
- Freitag M., Benz W., 2002, *A&A*, 394, 345
- , 2005, *MNRAS*, 358, 1133
- Fulbright M. S., Benz W., Davies M. B., 1995, *Astrophys. J.*, 440, 254
- Gafton E., Rosswog S., 2019, *MNRAS*, 487, 4790
- Gallego-Cano E., Schödel R., Dong H., Noguera-Lara F., Gallego-Calvente A. T., Amaro-Seoane P., Baumgardt H., 2018, *A&A*, 609, A26
- Gezari S., Chornock R., Rest A., Huber M. E., Forster K., Berger E., Challis P. J., Neill J. D., Martin D. C., Heckman T., Lawrence A., Norman C., Narayan G., Foley R. J., Marion G. H., Scolnic D., Chomiuk L., Soderberg A., Smith K., Kirshner R. P., Riess A. G., Smartt S. J., Stubbs C. W., Tonry J. L., Wood-Vasey W. M., Burgett W. S., Chambers K. C., Grav T., Heasley J. N., Kaiser N., Kudritzki R.-P., Magnier E. A., Morgan J. S., Price P. A., 2012, *Nat*, 485, 217
- Gezari S., Halpern J. P., Komossa S., Grupe D., Leighly K. M., 2003, *ApJ*, 592, 42
- Guillochon J., Ramirez-Ruiz E., 2013, *ApJ*, 767, 25
- Hills J. G., 1975, *Nat*, 254, 295
- Holoien T. W. S., Prieto J. L., Bersier D., Kochanek C. S., Stanek K. Z., Shappee B. J., Grupe D., Basu U., Beacom J. F., Brimacombe J., Brown J. S., Davis A. B., Jencson J., Pojmanski G., Szczygiel D. M., 2014, *MNRAS*, 445, 3263
- Ivanov P. B., Chernyakova M. A., 2006, *A&A*, 448, 843
- Kesden M., 2012, *Phys. Rev. D*, 85, 024037
- Khabibullin I., Sazonov S., Sunyaev R., 2014, *MNRAS*, 437, 327
- Kippenhahn R., Weigert A., 1994, *Stellar Structure and Evolution*. Springer-Verlag Berlin Heidelberg
- Krolik J., Piran T., Ryu T., 2020, *arXiv e-prints*, arXiv:2001.03234
- Kupi G., Amaro-Seoane P., Spurzem R., 2006, *MNRAS*, L77+
- Lai D., Rasio F. A., Shapiro S. L., 1993, *ApJ*, 412, 593
- Li L.-X., Narayan R., Menou K., 2002, *ApJ*, 576, 753
- Magorrian J., Tremaine S., 1999, *MNRAS*, 309, 447
- Miles P. R., Coughlin E. R., Nixon C. J., 2020, *arXiv e-prints*, arXiv:2006.09375
- Murphy B. W., Cohn H. N., Durisen R. H., 1991, *ApJ*, 370, 60
- Nandra K., Barret D., Barcons X., Fabian A., den Herder J.-W., Piro L., Watson M., Adami C., Aird J., Afonso J. M., et al., 2013, *ArXiv e-prints*
- Noble S. C., Krolik J. H., Hawley J. F., 2009, *ApJ*, 692, 411
- Peters P. C., 1964, *Physical Review*, 136, 1224
- Peters P. C., Mathews J., 1963, *Physical Review*, 131, 435
- Piran T., Svirski G., Krolik J., Cheng R. M., Shiokawa H., 2015, *ApJ*, 806, 164
- Price D. J., 2007, *Publications of the Astronomical Society of Australia*, 24, 159
- Rasio F. A., 2000, *Progress of Theoretical Physics Supplement*, 138, 609
- Rees M. J., 1988a, *Nat*, 333, 523
- , 1988b, *Nat*, 333, 523
- Reynolds C. S., 2014, *Space Science Reviews*, 183, 277
- Ryu T., Krolik J., Piran T., Noble S. C., 2020a, *arXiv e-prints*, arXiv:2001.03501
- , 2020b, *arXiv e-prints*, arXiv:2001.03502
- , 2020c, *arXiv e-prints*, arXiv:2001.03503
- , 2020d, *arXiv e-prints*, arXiv:2001.03504
- Schödel R., Gallego-Cano E., Dong H., Noguera-Lara F., Gallego-Calvente A. T., Amaro-Seoane P., Baumgardt H., 2018, *A&A*, 609, A27
- Servin J., Kesden M., 2017, *Phys. Rev. D*, 95, 083001
- Shapiro S., Teukolsky S., 1983, *Black holes, white dwarfs, and neutron stars: The physics of compact objects*. Wiley-

- Interscience
- Springel V., 2005, MNRAS, 364, 1105
- Stone N. C., Vasiliev E., Kesden M., Rossi E. M., Perets H. B., Amaro-Seoane P., 2020, Space Science Reviews, 216, 35
- Syer D., Ulmer A., 1999, MNRAS, 306, 35
- Tagoshi H., Ohashi A., Owen B. J., 2001, Ph. Rv. D., 63, 044006
- Tejeda E., Gafton E., Rosswog S., Miller J. C., 2017, MNRAS, 469, 4483
- van Velzen S., Farrar G. R., 2014, ApJ, 792, 53
- van Velzen S., Gezari S., Hammerstein E., Roth N., Frederick S., Ward C., Hung T., Cenko S. B., Stein R., Perley D. A., Taggart K., Sollerman J., Andreoni I., Bellm E. C., Brinnel V., De K., Dekany R., Feeney M., Foley R. J., Fremling C., Giomi M., Golkhou V. Z., Ho A. Y. Q., Kasliwal M. M., Kilpatrick C. D., Kulkarni S. R., Kupfer T., Laher R. R., Mahabal A., Masci F. J., Nordin J., Riddle R., Rusholme B., Sharma Y., van Santen J., Shupe D. L., Soumagnac M. T., 2020, arXiv e-prints, arXiv:2001.01409
- Wang J., Merritt D., 2004, ApJ, 600, 149
- Wheeler J., 1971, in Study Week on Nuclei of Galaxies, O'Connell D. J. K., ed., p. 539
- Will C. M., 2018, Theory and Experiment in Gravitational Physics, 2nd edn. Cambridge University Press
- Zhou Z. Q., Liu F. K., Komossa S., Cao R., Ho L. C., Chen X., Li S., 2020, arXiv e-prints, arXiv:2002.02267